This article has been accepted for publication in a future issue of this journal, but has not been fully edited. Content may change prior to final publication. Citation information: DOI 10.1109/TMI.2014.2383835, IEEE Transactions on Medical Imaging

Transcranial Assessment and Visualization of Acoustic Cavitation: Modeling and Experimental Validation

Costas D. Arvanitis*, Gregory T. Clement, and Nathan McDannold

***Abstract*—The interaction of ultrasonically-controlled microbubble oscillations (acoustic cavitation) with tissues and biological media has been shown to induce a wide range of bioeffects that may have significant impact to therapy and diagnosis of central nervous system diseases and disorders. However, the inherently non-linear microbubble oscillations combined with the micrometer and microsecond scales involved in these interactions and the limited methods to assess and visualize them transcranially hinder both their optimal use and translation to the clinics. To overcome these challenges, we present a noninvasive and clinically relevant framework that combines numerical simulations with multimodality imaging to assess and visualize the microbubble oscillations transcranially.**

In the present work, acoustic cavitation was studied with an integrated US and MR imaging guided clinical FUS system in non-human primates. This multimodality imaging system allowed us to concurrently induce and visualize acoustic cavitation transcranially. A high-resolution brain CT-scan that allowed us to determine the head acoustic properties (density, speed of sound, and absorption) was also co-registered to the US and MR images. The derived acoustic properties and the location of the targets that were determined by the 3D-CT scans and the post sonication MRI respectively were then used as inputs to two- and three-dimensional Finite Difference Time Domain (2D, 3D-FDTD) simulations that matched the experimental conditions and geometry. At the experimentally-determined target locations, synthetic point sources with pressure amplitude traces derived by either a Gaussian function or the output of a microbubble dynamics model were numerically excited and propagated through the skull towards a virtual US imaging array. Then, using passive acoustic mapping that was refined to incorporate variable speed of sound, we assessed the losses and aberrations induced by the skull as a function of the acoustic emissions recorded by the virtual US imaging array. Next, the simulated passive acoustic maps (PAMs) were compared to experimental PAMs. Finally, using clinical CT and MR imaging as input to the numerical simulations, we evaluated the clinical utility of the proposed framework.

The simulations indicated that the diverging pressure waves propagating through the skull lose 95% of their intensity as compared to propagation in water-only. Further, the incorporation of a variable speed of sound to the PAM back-projection algorithm indeed corrected the aberrations introduced by the skull and substantially improved the resolution. More than 94% agreement in the FWHM of the axial and transverse line profiles between the simulations incorporating microbubble emissions and experimentally-determined PAMs was observed. Finally, the results of the 2D simulations that used clinical datasets are promising for the prospective use of transcranial PAM in a human with an 82 mm aperture broadband linear array. Incorporation of variable speed of sound to the PAM back-projection algorithm appeared capable of correcting the aberrations introduced by the human skull.

These results suggest that this integrated approach can provide a physically accurate and clinically-relevant framework for developing a comprehensive treatment guidance for therapeutic applications of acoustic cavitation in the brain. Ultimately it may enable the quantification of the emissions and provide more control over this nonlinear process.

***Index Terms*— Acoustic Cavitation, Image Guided Therapy, Focused Ultrasound, Numerical Modeling, Multimodality Imaging**

I. INTRODUCTION

Ultrasonically-controlled stable and inertial microbubble oscillations (acoustic cavitation) exert forces that can, among others, activate cell's mechanoreceptors[1], disrupt cellular and vascular membranes[2]–[4], accelerate the dissolution of blood clots[5], enhance thermal ablation[6], [7] and induce localized tissue erosion[8]. Harnessing these abilities holds great promise for therapy and diagnosis of central nervous system diseases and disorders[9], [10]. Here, in order to utilize this potential, we present a noninvasive and clinically relevant framework that combines numerical simulations with multimodality imaging to assess and map microbubble oscillations transcranially.

Oscillating microbubbles under time varying acoustic field can be treated as point sources that emit strong diverging spherical pressure waves (as much as ~ 10kPa)[11] that are rich in harmonic, ultra- and sub-harmonic emissions of the excitation frequency, and at high pressures, broadband emissions[12]. Prior work has associated harmonic emissions, an inherent characteristic of nonlinear oscillators, with stable microbubble oscillations. Emissions at ultra- and sub-harmonics also tend to appear with stable cavitation, whereas broadband emissions are considered as an indication of inertial cavitation[13]. The appearance of these spectral components

Manuscript received October 20, 2014; revised December 09, 2014; accepted December 10, 2014. Date of publication xx, xxxx; This work was supported by the NIH grants K99EB016971, R25CA089017, P01CA174645, P41EB015898. Asterisk indicates corresponding author.

*C. D. Arvanitis at the Department of Radiology, Brigham and Women's Hospital, Harvard Medical School, Boston, Massachusetts, USA (e-mail: cda@bwh.harvard.edu).

G. T. Clement is at the Department of Biomedical Engineering, Cleveland Clinic, Cleveland, Ohio, USA e-mail: clemeng@ccf.org).

N. McDannold is with the Department of Radiology, Brigham and Women's Hospital, Harvard Medical School, Boston, Massachusetts, USA (e-mail: njm@bwh.harvard.edu).

in the emissions, which can be readily recorded with piezoelectric elements operated in passive mode [14], [15], can be used to establish a link between the prevalence of a particular type of oscillation (stable or inertial) and a specific bioeffect[16]–[18]. Despite high tissue attenuation, these high frequency components can also be recorded in vivo[19]–[23].

Recently, synchronously-operated arrays of passive cavitation detectors (typically 64-128 elements) in combination with appropriate reconstruction techniques[24] have enabled passive acoustic mapping of cavitation activity[25], [26]. This mapping, which can be performed for specific frequency bands using frequency domain reconstructions[27], can produce higher sensitivity than single element detection since the signal to noise ratio is proportional to the square root of the number of elements[28]. Passive acoustic mapping has successfully been used in phantoms and animal studies to visualize stable and inertial cavitation in soft tissues and in the brain transcranially[29]–[32]. For the latter, aberrations of the acoustic field caused by the skull can be corrected using hydrophone measurements[33]. These corrections have also been performed in silico using anatomical information from CT scans [28]. Such model-based correction algorithms are similar to those developed to improve focusing in transcranial MRI-guided focused ultrasound (FUS) systems[34], [35]. Recently, we integrated an US imaging array within a clinical transcranial MRI-guided FUS, which enabled concurrent spatio-temporal assessment and co-localization of both the mechanical and thermal effects of acoustic micro-cavitation with its associated bioeffects [31], [36].

It would be desirable to quantify the strength of acoustic emissions in addition to simply localizing the cavitation activity and characterizing it as either stable or inertial. To do this, one needs to have knowledge about the acoustic losses experienced during propagation. In our prior work, using a single element passive cavitation detector, we developed a semiquantitative method that used the strength of the emissions relative to background signals that were acquired without microbubbles. This measurement was found to correlate well with the level of blood-brain barrier permeabilization in experiments in non-human primates (NHP)[21]. In a separate study, we showed that the location of cavitation activity identified by the passive acoustic maps (PAMs) agreed with the location of the resulting MRI-evident blood-brain barrier permeabilization[31]. Despite these encouraging data, the presence of outliers in these experiments, which have also been reported in other studies[32], and the challenges involved in understanding their origin, underscored the need to simulate the entire procedure. We anticipate that such simulations will allow us to i) study the propagation of the acoustic emissions through tissues and skull, ii) assess the losses involved, and iii) understand how these losses could have affected the above data, allowing us to eventually account for them. Our general hypothesis is that the strength of the microbubble emissions, which echo the strength of the oscillations and thus the forces exerted to surrounding cells and vessels by the oscillations, can, for example, be used to modulate the level of the BBB disruption non-invasively. This methodology will eventually allow us to test it.

Finite Difference Time Domain (FDTD) methods are well-suited to modeling sound propagation in tissues and therefore can be used to accomplish the above tasks. While FDTD methods require greater computational time and memory, for example, as compared to pseudospectral methods [37], [38], they have several features that make them attractive for the present study. In particular, their ability to directly discretize the governing equations and to incorporate both heterogeneous media (such as the complex internal structure of the skull) and broadband point sources as well as their relatively easy implementation are significant advantages that the present work exploits. Previously, numerical simulations based on FDTD methods have been used for i) estimating the FUS induced heating upon finite amplitude sound propagation [39], ii) the evaluation of time reversal acoustics for transcranial focusing [35], and iii) the thermal deposition in skull during FUS [40]. In the present work, a full three-dimensional FDTD simulation for heterogeneous absorbing mediums was used in order to assess the losses and aberrations introduced by the skull and brain tissue on the microbubble acoustic emissions. To do so, we extracted the head properties from CT data, as previously shown [35], incorporated synthetic point sources using either Gaussian functions or pressure-time data derived by microbubble dynamics models[41], [42] and then numerically propagated them towards a virtual US imaging array. The data received by the virtual array were then used as inputs to a time domain PAM back-projection algorithm[43] that was modified to incorporate a variable speed of sound. Finally, the PAM intensity and resolution were compared to simulations without the skull and brain tissue to assess the losses and aberration to the received data.

In conjunction with the 3D-FDTD simulations, we developed a three modality imaging approach (2D-US, 3D-MRI, and 3D-CT) to improve our ability to assess and visualize acoustic cavitation in the brain in vivo. While the use of three different modalities may seem excessive, they each provide distinct information. Specifically, they allowed us to noninvasively i) characterize and map acoustic cavitation (US/PAM), ii) identify the brain structures and targeted region and visualize its bioeffects (MRI), and iii) account for spatially varying wave propagation effects, such as refraction and diffraction (CT). In addition, the material properties and sonication targets extracted from the co-registered CT and MRI datasets, which were used as inputs to the 3D-FDTD simulations, enabled the development of physically accurate simulations and, within registration limits, matching the simulations with the experiments. The simultaneous use of these abilities has not been shown before to our knowledge.

The purpose of this study was to evaluate this 3D-FDTD method and multimodality imaging approach for passive acoustic mapping during transcranial microbubble-enhanced sonication. We used these tools to simulate the passive acoustic maps obtained in a previous study of FUS-induced blood-brain barrier (BBB) disruption in nonhuman primates

(NHP)[31]. We then estimated the effects of the skull on the maps and evaluated whether these effects could explain some of the extraneous findings in that study. Finally, we investigated the feasibility of scaling the method up for passive acoustic mapping through the thicker human skull by creating simulated maps based on anatomical information obtained from CT and MRI of a brain tumor patient from a prior study[44].

II. MATERIAL AND METHODS

A. *Numerical Simulations*

The low intensity and diverging nature of a microbubble's acoustic emissions minimizes the possibility for finite amplitude effects. Therefore, to model acoustic propagation we combined the linearized equations of continuity, momentum, and state, and by invoking Stokes assumption $\left(\lambda+2\mu=4/3\,\mu\right)$, the following differential equations that govern linear acoustic propagation in heterogeneous, thermoviscous media is derived [45]:

$$\frac{\partial u(r,t)}{\partial t}=-\frac{1}{\rho_0(r)}\cdot\left(1-\mu'(r)\cdot\frac{\partial}{\partial t}\right)\cdot\nabla p(r,t) \tag{1}$$

$$\frac{\partial p(r,t)}{\partial t}=-\rho_0(r)\cdot c_0^2(r)\cdot\nabla u(r,t) \tag{2}$$

where

$$\mu'=\frac{4}{3}\cdot\frac{\mu}{\rho_0\cdot c_0^2} \tag{3}$$

$$\mu=\delta\cdot\rho_0 \tag{4}$$

$$\delta=\frac{2\cdot\alpha\cdot c_0^3}{\omega^2} \tag{5}$$

by combining Eqs. 3, 4 and 5 we get:

$$\mu'=\frac{8}{3}\cdot\frac{\alpha\cdot c_0}{\omega^2} \tag{6}$$

where, p is the pressure, u is the particle velocity, r is a point in space, α is the absorption in Np.m^{-1}, c_0 is the linear speed of sound in m.s^{-1}, ρ_0 is the density kg.m^{-3}, μ is shear viscosity in kg.s^{-1}·m^{-1}, λ is the dilatational viscosity coefficient, δ is the kinematic viscosity in m^2.s^{-1}, and ω is the angular frequency in radians,. Eq. 5 expresses the momentum diffusivity δ as a function of the absorption coefficient α [46]. The material properties of the brain tissue and skull (ρ_0, c_0, and α) were extracted from high-resolution 3D-CT data and semi-empirical models, as described in section II.C. With this formulation, the acoustic intensity can be directly computed from the particle velocity.

Equations 1 and 2 were discretized and solved numerically in 3D using the staggered-grid technique[47], [48]. The present implementation is first order accurate in time and second order accurate in space. A square uniform Cartesian mesh that secured conformity to the data from the imaging systems was used. A fine grid was used to minimize numerical dispersion [47]:

$$\frac{\max\left(c_0(r)\right)}{f_0 dx}>10 \tag{7}$$

for the simulations with the NHP and clinical data, $dx=dy=dz=125\,\mu m$ and $dx=dy=dz=100\,\mu m$ were used respectively, while the time step was set so as to satisfy Courant condition [49]:

$$dt<\frac{dx}{\sqrt{D}\cdot\max\left(c(r)\right)}\cdot\frac{1}{1+\omega^2\cdot\max\left(\mu(r)\right)^2/4} \tag{8}$$

However, in the presence of strong absorption by the skull, the requirement of $\omega\cdot\max\left(\mu(r)\right)<<1$ imposes an upper limit on μ for the frequencies tested here (<1.5 MHz). Thus, to ensure stability we used a time step (dt) that was 45% smaller than the upper limit described by the Courant condition. In addition, second order absorbing boundary conditions were found to be adequate for reducing reflections from the boundaries (see supplementary video 1, 2D-FDTD). Secondary effects such as mode conversion and shear waves were ignored in the current implementation.

Two different synthetic point sources were used in the simulations. The first was based on microbubble emissions that were determined using the Bubblesim simulation tool[42]. Bubblesim solves the Rayleigh-Plesset equation with radiation damping using the approach originally developed by Church[41]. For the determination of the microbubble emissions, the frequency of the excitation pulse in the model was set to 0.44 MHz (Figure 1 A), which resulted to 2nd harmonic at 0.88 MHz and 3rd harmonic at 1.32 MHz. To minimize numerical dispersion (Eq. 7), the excitation pulse amplitude was selected so as the maximum frequency in the emissions was less than 1.5 MHz (i.e. 3rd Harmonic).

Note that in the simulated emissions the excitation frequency was absent. So, while these data match only the 2nd, 4th, and 6th harmonic of our experimental data (Fig. 3) they do, however, have significant overlap with the experimental data, where the excitation frequency (220 kHz) was filtered out (high pass digital filter with Fc=330 kHz) by the recorded acoustic emissions. This tradeoff also allowed to avoid unnecessary filtration in the simulated data, while retaining higher harmonics without entering into the inertial cavitation regime that would introduce strong broadband emissions and lead to significant numerical dispersion in the simulations. Also, these frequencies span over a frequency range that is relevant to transcranial ultrasound propagation and are relevant to the emissions generated by the excitation frequencies of current clinical systems (220 kHz and 660 kHz). In the simulations with the microbubble emissions the absorption, α, was set equal to zero as methods to model arbitrary attenuation, such as methods with relaxation mechanisms [50], were not included in the current implementation.

The other synthetic point source was generated using the "gauspuls" function in Matlab (The MathWorks, Natick, MA, USA) (Figure 1 A). This point source was set to have central frequency of 0.44 MHz, 0.88 MHz, or 1.32 MHz. As before, these frequencies matched the even harmonics of our experimental data. The relatively narrow bandwidth (60%) of this point source allowed us to assess, in separate simulations, the losses and aberration of the acoustic emissions, as they propagated through the skull and towards the receivers, at different frequencies. In these simulations the attenuation was incorporated and, for the different frequencies tested, was scaled with an f^1 frequency dependence.

Example amplitude traces and spectra from the two different synthetic point sources and representative snapshots from the 3D-FDTD simulations with the NHP datasets are shown in Figure 1. The location of the point source and linear US imaging array at the temple are also shown (see below for more details). As can be seen, the emissions from the point sources aberrate through the skull and then reflect and scatter as they propagate outwards before a part of the transmitted energy is collected by the US imaging array. The data recorded by the US imaging array data are then back-projected into the image space to form PAMs as described in the next section. The amplitude of the point sources was determined by their spectra (Figure 1 A bottom) and was equal in all simulations.

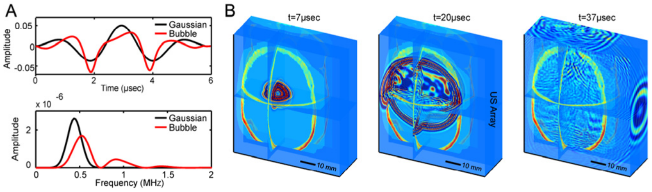

Fig. 1.Three-Dimensional Finite Difference Time Domain simulations. (A) Synthetic point sources trace amplitude (top) and spectra (bottom) generated by a Gaussian pulse (3 cycles, 440 kHz, 60% bandwidth) or using the Rayleigh-Plesset model with radiation damping (2.5 cycles). The following parameters were used with this microbubble model: pulse amplitude: 130 kPa, pulse length: 2.5 cycles, pulse center frequency: 440 kHz, bubble radius: 2 μm, shell thickness: 20 nm, shell shear modulus: 11.6 MPa, shell viscosity: 0.48 Pa·s. (B) Different times showing the propagation of the diverging pressure waves with the 3D-FDTD simulations. The computational grid had 700 × 830 × 400 nodes. A Gaussian synthetic point source (0.88 MHz) was used in this example. The 3D-FDTD with a synthetic point source based on microbubble emissions is shown in supplementary video 2.

B. Passive Acoustic Mapping with Variable speed Of Sound

The underlying idea in passive acoustic mapping is to exploit the coherent acoustic emissions recorded by passive receivers to form maps proportional to the strength of the emissions, here produced by the microbubble oscillations. In particular, the diverging pressure wave emitted from each bubble can be modeled as being emitted by a point source $s(r,t)$ (since the smallest radiated wavelength >> maximum bubble size) originating from position $r(x,y,z)$. If these emissions are recorded at locations r_n of N transducers, then the location of the point source can be estimated by coherently summing the recorded acoustic emissions $u(r_n,t)$ in (r,t) space, with $t=|r-r_n|/c_0$ and c_0 the sound speed between the bubble and the transducer elements, as follows:

$$s(r)=\sum_{n=1}^{N}|r-r_n|\cdot u_n\left(r_n,\frac{|r-r_n|}{c_0}\right) \tag{9}$$

where the $|r-r_n|$ term describes geometric wavefront loss. For the linear array that was considered here, the 3D vectors r are converted to image coordinates x (transverse) and z (axial) $(y=0)$ as follows:

$$\left(|r-r_n|=\sqrt{(x-x_n)^2+z^2}\right) \tag{10}$$

It is evident that this back-propagation algorithm requires knowledge of the speed of sound of the media between each point in the image and each receiver [24]. While prior work has assumed uniform speed of sound[24], [26], this assumption does not hold for transcranial propagation. The average (or effective) speed of sound $\bar{c}_{0,n}$ between each point in the image and the n^{th} receiver can be determined according to the following equation[36]:

$$\bar{c}_{0,n}=\sum_{i=1}^{M}\frac{d_i}{L}c_{0,i} \tag{11}$$

where d_i and $c_{0,i}$ are the thickness and sound speed, respectively, of the M different media in the beam path (i.e. tissue, skull, water, etc,), L is the total propagation distance (i.e. Euclidean distance between the point and each receiver), and $\bar{c}_{0,n}$ being the effective speed of sound between each point in the image r and each receiver r_n. Then, the relative point source intensity $I(r)=|s(r)|^2$, after subtracting incoherent background noise (i.e. the DC component)[24] is given by:

$$I_n(r)=\left|\sum_{i=1}^{N}|r-r_n|\cdot u_n\left(r_n,\frac{|r-r_n|}{\bar{c}_{0,n}}\right)\right|^2 -\sum_{i=1}^{N}\left||r-r_n|\cdot u_n\left(r_n,\frac{|r-r_n|}{\bar{c}_{0,n}}\right)\right|^2 \tag{12}$$

The maps formed with Eq. 12 are linear in intensity as long as the point sources are spatially incoherent. Although this assumption may be violated when secondary Bjerknes forces between oscillating microbubbles are present, we assumed that the microbubble distribution will be sparse, preventing bubble-bubble interactions, and the amplitude of oscillations is relatively small [51], [52], which is true for most clinical applications of interest. This algorithm also does not account for shear waves and mode conversion, which has been included in formulations based on multi-layered ray acoustic transcranial ultrasound propagation[28]. It does, however, incorporate all first order effects and is also more computationally efficient. Since $\bar{c}_{0,n}$ was estimated independently for each receiver from CT data (see next section), the effects of refraction and diffraction are implicitly included. Therefore, including these spatially varying effects in Eq. 12 improves the resolution and provides more accurate spatial information.

C. Image Acquisition, Registration, and Quantification

The NHP experiments utilized data from three different modalities: US, MRI and CT. MRI and US imaging were acquired during the experiments (see section II.D), whereas the CT scans were obtained several days beforehand. The US imaging array was at a fixed location throughout the experiments, and we used B-mode images (central frequency: 3.21 MHz; resolution 1.25×1.25 mm) of MRI fiducial markers for US/MRI registration. MRI acquisitions included a 3D T1-weighted gradient echo sequence (TR/TE/TI: 5.3/2/600 ms; flip angle: 10°; field of view (FOV): 12.8 cm; matrix: 128×128; slice thickness: 2 mm) for imaging the MRI fiducial markers and for treatment planning, a T2-weighted fast spin echo (FSE) sequence (TR/TE 4500/85 ms; echo train length: 8; FOV: 12 cm; matrix: 256×256; slice thickness: 3 mm) for anatomy, and T1-weighted FSE sequence (TR/TE: 500/14 ms; echo train length: 4; FOV: 12 cm; matrix: 256×256, slice thickness: 3 mm) to detect signal enhancement indicating BBB disruption after IV administration of the MRI contrast agent Gd-DTPA (Magnevist, Berlex; dose: of 0.1 mmol/kg). The location of the contrast enhancement (Figure 2 A-Left) at the different sonication targets was used as the point source in the simulations. The CT scans (Figure 2 A-Right) (Ceretom, Danvers, MA, USA) were reconstructed with a voxel volume of 0.49×0.49×0.65 mm using a bone kernel to obtain the skull and tissue densities.

Before the sonications, MR and B-mode US images (128 elements) of fiducial markers were used to determine the transformation matrix between the two imaging coordinate systems. The MR fiducial markers used (Beekley, MR-SPOTS, MRI skin markers, 122) were plastic cylindrical capsules (R: 3 mm, length: 15 mm) filled with an MR-visible liquid that were also visible in US imaging. The base of the capsules was attached at the vertices of a perpendicular triangle (20 mm base and 40 mm height) and positioned into the US imaging plane (coronal plane, see also Fig. 3). After collecting the US and MR images with resolution higher than the capsule's cross section (6 mm), we identified manually the center of each capsule and determined the transformation matrix (rotate and shift) between the two imaging coordinate systems. Prior to registration, the images were interpolated in order to have the same in-plane voxel dimensions (0.3 mm). The registration accuracy was dictated by our ability to determine the center of the fiducial markers in US and MR images (X-Y directions) as well as our ability to match the US and MRI planes (Z-direction). In X-Y directions the FWHM of the fiducial markers in MRI images was 3.6±0.5 mm and the separation of the walls in US images was 5.9±0.6 mm. So, we expect that the resolution in X-Y plane was at best 3.6 mm. In the Z direction the registration accuracy was determined by the absence in the US and MR images with the three capsules of a capsule (6 mm) that was attached horizontally to the holder of the capsules[53]. We expect that the registration in Z-direction was better than 9 mm. At the end of the registration we visually confirmed the registration accuracy using the NHP anatomic images (Fig. 2A-Middle & 2B-Left) obtained before the sonications and confirming that the head US images were aligned with the MRI images.

Rigid body registration was performed between T2-weighted FSE MRI and CT scans using 3D-Slicer (version 4.1; www.slicer.org) for both the NHP and clinical data. To facilitate the simulations, we used b-spline interpolation with this software to produce registered MRI and CT scans with isotropic voxel dimensions of 0.47 and 0.4 mm for the NHP and human data, respectively. Note that the interpolation to 0.4 mm was performed to obtain iso-voxels in the CT data for the numerical simulations, rather than improve our registration accuracy, which would require higher resolution images. Finally, CT/US registration was achieved using the transformation matrices from the previous two registrations, thus the resolution accuracy of this registration should not be better than the accuracy of the other registrations. Figure 2B shows the fused images from the three modalities.

The densities of the skull and the brain were determined by the registered CT data, while other acoustic properties were obtained using empirical models based on skull porosity, Ψ,[35], [37], [54] as follows:

$$\Psi = 1 - \frac{\mathrm{H}}{1000}, \tag{13}$$

$$c = \mathrm{c}_{water}\Psi + \mathrm{c}_{bone}\left(1-\Psi\right), \tag{14}$$

$$abs = \mathrm{abs}_{\min} + \left(\mathrm{abs}_{\max} - \mathrm{abs}_{\min}\right)\times\Psi^{\beta}, \tag{15}$$

where H is the Hounsfield unit, c_{water} is the speed of sound in water, c_{bone} is the maximum speed of sound in the skull (set to be 2500 $\mathrm{m.s^{-1}}$ for human and 3100 $\mathrm{m.s^{-1}}$ for NHP), abs is the absorption coefficient, and $abs_{\min}$ and $abs_{\max}$ (set to be 0.0675 and 2.7 dB $\mathrm{mm^{-1}}$, respectively both for human and NHP). To convert abs to the diffusivity δ, we used Eq 5. Finally, β is set to be 0.5 [35]. The choices for these acoustic parameters come from the available literature (for more detail see Table I).

This article has been accepted for publication in a future issue of this journal, but has not been fully edited. Content may change prior to final publication. Citation information: DOI 10.1109/TMI.2014.2383835, IEEE Transactions on Medical Imaging

TABLE I
SKULL, BRAIN, AND WATER PROPERTIES USED IN THE SIMULATIONS.

PROPERTIES	DEGASSED WATER	BRAIN TISSUE	SKULL
Density ($kg \cdot m^{-3}$)	1000	1300 [40]	From CT images 1400-2200 [54]
Speed of Sound (m/sec^{-1})	1480 at 19°C [57]	1562 [58]	1500-3100 for NHP and 1500-2500 for human [35], [54], [59]
Absorption ($Np \cdot m^{-1}$)	2.9×10^{-4} [60]	2.9 at 0.75 MHz [40]	5.9-234.5 at 0.8 MHz[35], [37], [54], [59]

For the tissues outside the skull (skin, fat, muscle) we used the properties of brain tissue. Table I shows the actual values along with the references from which these values were taken. Figure 2 C shows the quantitative images with the range of the different parameters based on the NHP CT datasets. Only the skull properties varied, the brain tissue properties were kept constant (see Table I for actual values). Also based on the semi-empirical models in the literature and values for the NHP and Human skull the former had higher attenuation (max attenuation for NHP and human skull was 234.5 vs 191 $Np \cdot m^{-1}$ respectively).

Before the determination of the material properties and in order to satisfy the conditions that minimized numerical dispersion (Eq. 7), the CT images were interpolated two times using Matlab's linear interpolation function. This interpolation resulted in voxel dimensions equal to 100 and 125 μm for the NHP and clinical data, respectively. It also blurred the edges between the skull and the neighboring tissue, so we excluded any voxel in the CT images that was less than 1400 $kg \cdot m^{-3}$. Voxels inside the skull that had density lower than this threshold were corrected manually on a point-by-point basis.

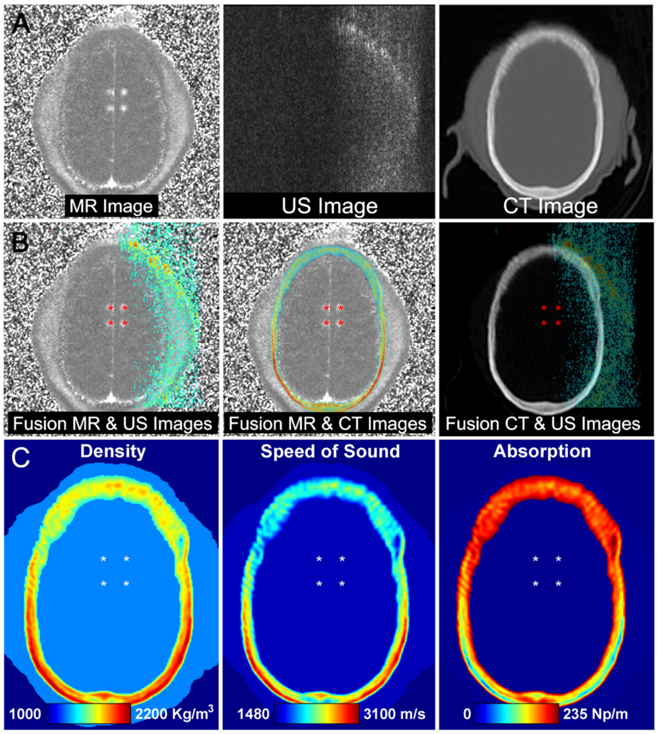

Fig. 2. Three modality image registration and acoustic properties of the NHP head. (A) Axial MRI, b-mode US imaging, and CT of an NHP. The MRI shows a map of the percent change in signal after administration of a MRI contrast agent. Four enhancing targets show localized FUS-induced BBB disruption. (B) Fusion of different images. (C) Quantitative images showing the range of the acoustic parameters from the NHP at 0.88 MHz. Similar values were extracted from the clinical data (See table I). The four stars indicate the locations of the BBB disruption in the MRI.

D. *Experimental Methods and Procedures*

Experimental data were acquired previously in a study in rhesus macaques that investigated passive acoustic mapping (without a variable speed of sound) during FUS-induced BBB disruption [31]. A clinical MRgFUS system (ExAblate 4000 low frequency, InSightec, Haifa, Israel), which was integrated with a clinical 3T MRI unit (GE Healthcare), was modified to provide the low-power sonications used for BBB disruption. This system, which uses a 1024-element phased array transducer, operates at a central frequency of 220 kHz and was driven in burst mode. The 30 cm diameter hemisphere transducer was oriented 90° from its normal clinical use so that it could be simply filled with degassed water like a bowl. Imaging was performed using a 15 cm surface coil with the animal placed supine on the MRI scanner table with its head partially submerged in water (Figure 3). For BBB disruption, a series of 10 ms bursts (100 bursts in total) were applied at a pulse repetition frequency of 1 Hz. Each sonication was combined with the microbubble US contrast agent Definity (Lantheus Medical Imaging, MA, USA), which was infused IV during the entire sonication via an MRI-compatible infusion pump (Spectra Solaris EP, Medrad, USA), as described before[55]. The microbubble agent was diluted in 5 ml sterile phosphate-buffered saline and infused over 100 s at a dose of 40 μl/kg.

A research US imaging system (Verasonics, Redmond WA, USA) was programmed in Matlab to operate in passive mode to acquire data for the PAMs; images were reconstructed offline. This system and the MRgFUS device were synchronized using an external trigger from an arbitrary waveform generator (Fluke, Everett, Washington, USA). The US imaging probe (L382, Acuson, WA, USA), which was available in our lab, was a 128-element (82 mm) linear array with a 3.21 MHz central frequency and a bandwidth of approximately 75%. The bandwidth of array has been selected to be away of the FUS excitation frequency, because we did not want to saturate our readout electronics (Verasonic's ADC). The ability to filter the data before ADC is not possible with the system that we currently have in the lab. Only half of the elements (every other element) were used since this particular model could synchronously read data only from 64 channels.

The array was incorporated into the therapeutic MRgFUS phased array with an acoustic mirror (Figure 3). The mirror size was larger than the array aperture and its projection covered the entire array profile. The array with the mirror was mounted to a 3D positioning system and it can, thus, move in the A-P (and S-I) direction, so PAM at different planes can be readily performed. It is noted that with this configuration different planes could be imaged by moving or changing the angle of the acoustic mirror. Before the experiments, fine-adjustments under real-time B-mode imaging allowed us to maximize the image intensity depicting the edges of a uniform cylindrical phantom, which presumably resulted to the best alignment between the US array and the reflector.

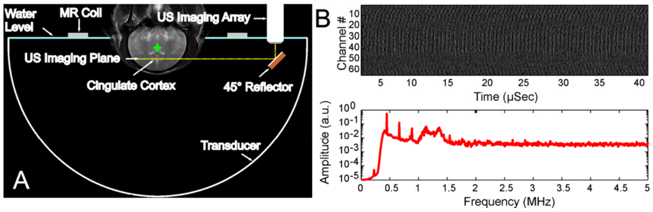

Fig. 3. Experimental setup. (A) Pre-sonication MRI of a macaque within the MRgFUS device with the integrated US imaging array. A coronal T2-weighted MR image has been annotated to show the location of the 30 cm diameter hemisphere MRgFUS transducer, the ultrasound imaging array that was connected to the research imaging engine, and the MRI surface coil. The annotations were drawn to scale with the location of the head in a typical position. A 45° brass reflector was used to create an axial imaging plane (yellow dotted line). The imaging array was located 13 cm away from FUS geometrical focus, similar to what might be used in a human. The green cross shows the geometric focus of the FUS transducer. The focal point could be moved to different brain targets without moving the transducer using the phased array for electronic beam steering. Inset, post-sonication contrast enhanced MRI in axial and sagittal planes; enhancing regions show successful BBB disruption (targeted locations). (B) Above: The voltage traces from the RF data recorded by the US array during the sonication (for clarity only 40 µsec are shown). Below: and average spectra of the emissions (64 elements). Note that no harmonic emissions were recorded by the array in the absence of microbubbles. The small bump in the spectra (1-1.5 MHz) is an artifact.

The first 180 µs of ultrasonic RF data were recorded for each burst (50 overall). The data were high-pass filtered (330 kHz cutoff frequency) to remove the 220 kHz MRgFUS frequency and then used to construct the cavitation maps according to Eq. 12 using the speed of sound extracted from the co-registered CT datasets. Both in the experimental and simulated data we have found that skull-related distortions appeared in the reconstructed PAMs (i.e. the outline of the skull; see Fig. 6A right). We also found that the PAM with the least distorted shape coincided with the less pronounced skull-related distortions. So, this metric was used to identify the CT slice to extract the speed of sound. In this work, the CT slice that provided the optimal PAM was identified by a colleague that was blinded to the experiments. The selected CT slice was found to be 1 mm in plane and 4 mm out of plane, which is within the registration accuracy limits. It is important to note that this step (i.e. identify the "best" CT slice) may be necessary irrespective of our registration accuracy, as we have observed that during the experiments the head of the NHP can move by as much as 2 mm from its original place. Note that identifying the PAM that provides the highest resolution or best shape, especially in the presence of skull aberrations, is not a good guide for identifying the best CT slice. For example, using the simulated data we found that 10 mm out off the plane emissions resulted to better image resolution, while still retaining "ideal" shape.

No comb filtering or rejection of any specific spectral band was used in the emissions. In the presence of broadband emissions, all possible types of oscillation, including inertial cavitation, will likely be present. Data from one animal at a sonicated target that that had strong harmonic emissions and broadband emissions was used. The acoustic power level was 1.3 W, which yielded an estimated peak negative pressure amplitude in the brain of 250 kPa[21].

In the simulations (implemented in Matlab), the RF data from the synthetic point sources (Figure 1 A) were numerically excited and propagated towards a virtual US imaging array that had the same aperture as the one we used in the NHP experiments. The array was located near the end of the simulation grid (i.e. 5 nodes before the absorbing boundary layers, 1.5 cm from the NHP skull) in the plane that we used for extracting the speed of sound in the experiments. The synthetic point source, whose in-plane coordinates were extracted from MRI, was also placed in this plane. 3D-FDTD simulations (Figure 1 B) were used to model the pressure field at the face of the virtual US imaging array. The collected data were binned to 64 elements and used as inputs to the passive acoustic mapping algorithm (Eq. 12). No other processing was performed. We created simulated passive maps with constant and variable sound speeds and assessed the losses and aberrations induced by the skull to the recorded acoustic emissions at different frequencies. We also compared maps generated by the two different synthetic point sources.

When we compared the synthetic PAM to the experiment we used 2D-FDTD simulations. In the experiments, the US imaging array was approximately 120 mm away from the point source, similar to what is to be expected under clinical conditions. This distance would require a grid with 1500×830×400 nodes (i.e. 150×83×40 mm), which could not be accommodated by the desktop computer (Dell Precision T7500 (64 bit) with two 2.53 GHz parallel processors and 12 GB memory) used in this study. For the same reasons, the simulations with human data were also performed in 2D (see supplementary video 3). The CT and MRI of the brain tumor patient were obtained in a clinical trial performed in our department [44]. In the 2D-FDTD simulations, the synthetic point source was based on emissions predicted by the microbubble model.

Overall, we simulated sonications at 4 targets in the NHP and one target in the human brain. In both cases, the distance between the point source and the imaging array was 120 mm. Note that although the distance of the array (not the mirror) from the geometrical focus of the FUS was 130 mm, we steered the beam, using the beam steering capabilities of the FUS systems, to sonicate a target that was 120 mm from the array. When evaluating the impact of different parameters (frequency, variable vs. constant sound speed) on the maps after propagation through the skull, comparisons were made to simulated PAMs after propagation through water only. Table II shows all the different permutations of the data presented here.

TABLE II
Summary of the experiments and simulations performed

Simulations	US Array - target distance	Simulations	Absorption	Displayed
3D - NHP	50 mm	Gaussian	Yes	Figure 4
3D - NHP	50 mm	Gaussian, Bubble	No	Figure 5
2D - NHP	120 mm	Bubble	No	Figure 6
2D - Human	120 mm	Gaussian	Yes	Figure 7

III. Results

A. *Three Dimensional Numerical Simulations*

First we assessed whether including a variable speed of sound (Eq. 12) can take into account spatially varying wave propagation affects. To do so, we utilized two separate full 3D-FDTD simulations using the synthetic point source with the Gaussian profile and a central frequency of 0.88 MHz. In the first, the synthetic point source was excited and numerically propagated, through water-only, towards the virtual US imaging array. In the second, it propagated through the brain, skull and water, as shown in Figure 1 B. From the PAMs formed from these simulations, we found that the diverging pressure waves propagating through the skull were significantly more distorted compared to water-only propagation (Figure 4 A, Left and Middle). Incorporating a variable speed of sound in the passive acoustic mapping back-projection algorithm indeed corrected the aberrations introduced by the skull (Figure 4 A Right), although not completely. The full width at half maxima (FWHM - 6dB) in the corrected PAMs was 29% and 38% larger than the PAMs formed by water-only propagation in the transverse and axial directions, respectively (Figure 4 B). In addition, the PAM with variable speed of sound correctly identified the location of the point source in both the axial and transverse locations despite the fact that a 2D back-projection reconstruction was used.

Apart from aberration, the skull also induced significant losses to the emissions. In particular, the PAM intensity formed using emissions that propagated through the skull was reduced by more than 95% compared to the water–only case. The peak PAM intensity was marginally improved by including a variable speed of sound in the PAM reconstructions. For the four different point source locations tested in the present study (Figure 2), which were separated by only 10 mm, the peak intensity varied by 20% or more in the PAMs with a constant speed of sound. Interestingly, this difference was reduced to less than 7% when a variable speed of sound was included. To investigate whether this small discrepancy was due to losses or aberrations induced by the skull, we examined the relationship between the FWHM, which also describes the energy spread, and the peak intensity. A linear correlation was observed with R^2=0.98, suggesting that this small disparity could be explained by skull aberrations only. These data suggest that this PAM back-projection algorithm that incorporates a variable speed of sound can substantially reduce the skull-induced aberrations and provide more accurate estimation of their losses. Therefore, unless otherwise specified, each PAM presented onwards include a variable speed of sound.

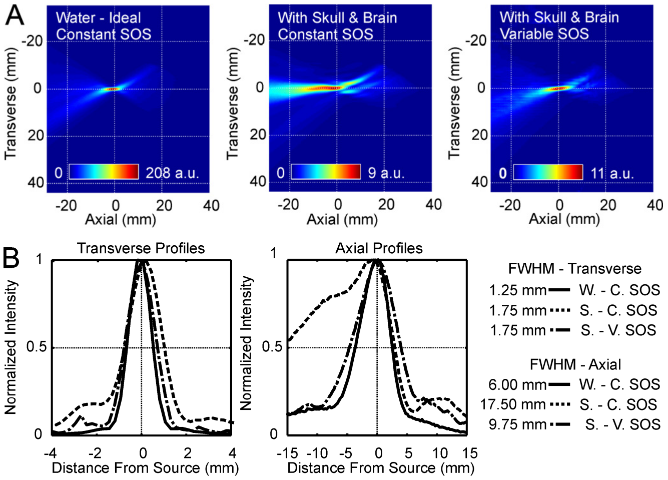

Fig. 4. Example PAMs and line profiles reconstructed from emissions created using the full 3D-FDTD simulations of the NHP. (A) PAMs formed after propagation through water only (left) and after propagation through brain, skull and water with (center) and without (right) the inclusion of a variable speed of sound (SOS). In each case the synthetic point source had a Gaussian profile, a central frequency of 0.88 MHz, and equal amplitudes. The location (0,0) is the coordinate of the point source. The near-field was on the right side of the image (i.e. the US imaging array was on the right). These simulations included absorption. (B) Normalized transverse and axial line profiles for the different conditions tested; i) water-only, constant speed of sound (W-C.SOS), ii) propagation through the skull, constant SOS (S-C.SOS), iii) propagation through the skull, variable SOS (S-V.SOS). For the second condition (S-C.SOS), we used an average speed of sound in the PAM back-projection algorithm determined by Eq. 11 and a distance between the location of point source and the center of the array of 5 cm. The values for the FWHM for the different conditions are provided in the figures.

Next, we measured the PAM resolution and intensity for different frequencies and the two different synthetic point sources (Figure 1 A). Since we used a single point source in each case, the FWHM values presented here are equivalent to the point spread function of our passive acoustic mapping algorithm for the simulation parameters (5 cm between the source and the imaging array, linear array with an 8.2 cm aperture) and frequencies examined. These FWHM values are good approximations of the transcranial resolution limits of the proposed PAM back-projection algorithm under these conditions. As expected, the spatial resolution improves with higher frequencies (Figure 5 B).

These data also suggest that transcranial PAM in the NHP at 1.32 MHz is feasible, however the higher distortions and increased loss due to reflections and scattering associated with mapping high frequency emissions make it challenging. Indeed, as can be seen from Figure 5, the PAM intensity dropped significantly with increasing frequency. For example, the peak PAM intensity at 1.32 MHz was 80% smaller than at

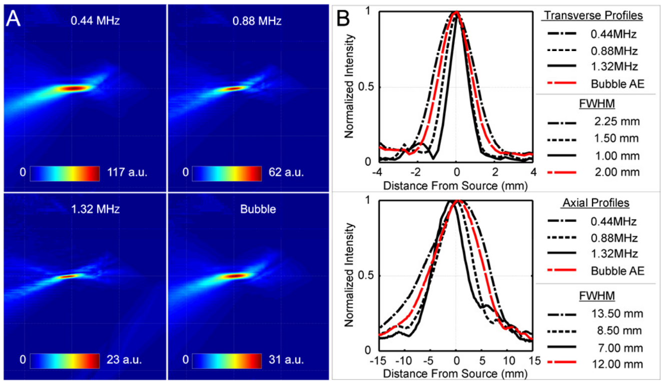

Fig. 5. Transcranial PAMs through a NHP skull with a variable speed of sound for simulated microbubble emissions at different frequencies and synthetic point sources. (A) reconstructed PAMs from emissions with different frequencies using a Gaussian point source and from emissions produced from microbubble dynamics model with an excitation frequency of 0.44 MHz. The amplitude of the two different synthetic point sources was set to be equal. Absorption was not included in these simulations. In all PAMs the near field is on the right hand side of the image. The location (0,0) is the coordinate of the point source. (B) Normalized transverse and axial line profiles from the PAMs. Values for the FWHM for the different conditions are provided in the figures.

0.44 MHz. Since absorption was ignored in these simulations this drop in intensity was directly related to losses due to multiple reflections and scattering. Although, a small numerical dispersion at higher frequencies might explain some of the differences, comparing the PAMs with and without absorption at 0.88 MHz, indeed, suggest that 70% of the total losses caused by propagation through the NHP skull were due to reflections and multiple scattering.

Finally, the PAM reconstructed with model-based microbubble acoustic emissions resembled the PAMs formed with the Gaussian point sources. While the FWHM of the PAM signal was primarily determined by the harmonic with the strongest amplitude (i.e. 1st harmonic: 0.44 MHz, see also Figure 1 A), the intensity was much lower than that of the Gaussian point source at 0.44MHz. This reduction occurred because a significant amount of the energy in the microbubble's acoustic emissions was at higher frequencies (see Figure 1 A, Top).

B. Two Dimensional Numerical Simulations

Having assessed the PAM with a variable speed of sound under different conditions, we then compared PAMs generated by a 2D-FDTD simulation to one obtained experimentally during microbubble-enhanced sonication in an NHP. In this simulation, the synthetic point source was located 12 cm from the imaging array and was derived from the microbubble dynamics model (excitation frequency: 0.44 MHz). As can be seen in Figure 6, the simulated and experimental PAMs have similar shapes and dimensions, with the FWHM of their transverse and axial line profiles differing by less than 6%. This agreement is notable since the simulated PAMs included components for only the 2nd, 4th, and 6th harmonics of our experimental data, suggesting that similar to the simulations above (Figure 5), the experimental PAM was dominated by the low frequency components.

Note that the resolution in these PAMs was greatly reduced compared to the simulations presented above due to the increased distance, 12 instead of 5 cm, between the point source and US imaging array. Further, despite the fact that the location of the synthetic point source and the location (but not the distance) of the US imaging array were identical with the one presented in Figure 4, these data had also much less distortions. This finding reflects the fact that as the array is moved further away from the head, the recorded emissions propagate through a smaller part of the skull, which in this case was relatively uniform with borders almost parallel to the US imaging array.

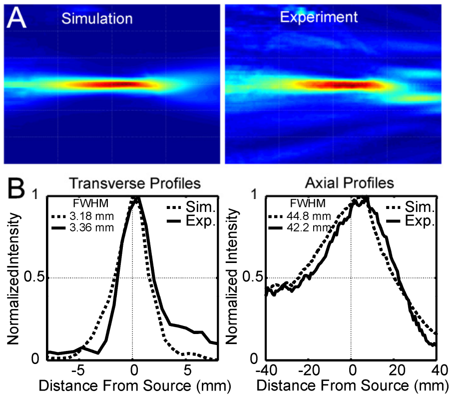

Fig. 6. Comparison of simulated (2D-FDTD) and experimental PAMs obtained transcranially during microbubble-enhanced sonication in an NHP. (A) Left: PAM reconstructed with a variable speed of sound from simulated acoustic emissions derived from a microbubble dynamics model with an excitation frequency of 0.44 MHz. Right: PAM with a variable speed of sound from an experiment. The acoustic emissions were recorded during a transcranial sonication at a frequency of 0.22 MHz. In both PAMs the near field was on the right (i.e. the US imaging array was on the right). (B) Normalized transverse and axial line profiles from the two PAMs. The FWHMs from the profiles of the two PAMs are also shown. The location (0,0) is the coordinate of the point source

Finally, we performed additional 2D-FDTD simulations with a clinical CT dataset (Figure 7). In these simulations, the emissions from the synthetic point source propagated towards the US imaging array through water-only or through brain, skull, and water. To be able to compare the simulated PAM intensity and resolution with those from the NHP, the imaging array and its position and distance (120 mm) from the synthetic point source (0.88 MHz with Gaussian profile) were kept the same. When a constant speed of sound was used for PAM reconstruction, the recorded emissions appeared to be shifted towards the US imaging array (Figure 7 B). Also, in the presence of absorption, a small secondary lobe in the far field that resembled weak cavitation activity was erroneously identified. In addition, the absorption appeared to reduce the image resolution by 6% (FWHM) in both directions. This reduction was due to a smaller effective aperture, as the waves recorded by the outermost elements traveled a longer distance and therefor experienced more losses. Incorporation of a variable speed of sound to the PAM back-projection algorithm corrected this artifact and improved the localization accuracy. The PAM intensity was reduced by only 7% compared to the

This article has been accepted for publication in a future issue of this journal, but has not been fully edited. Content may change prior to final publication. Citation information: DOI 10.1109/TMI.2014.2383835, IEEE Transactions on Medical Imaging

NHP simulations (data not shown), whereas the resolution in both directions was 32% worse. The small difference in the PAM intensity was also related to the higher skull attenuation used in the NHP simulations. Note that the NHP data are from 2D-FDTD simulations of a point source (880 kHz) located 120 mm from the array, not at the 50 mm used in the 3D simulations.

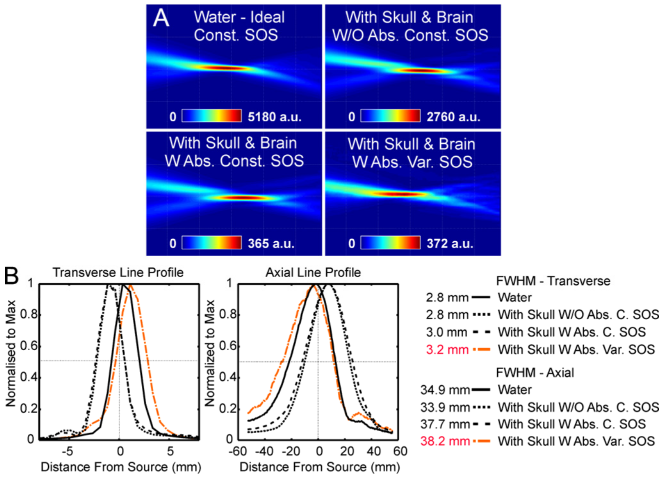

Fig. 7. Passive acoustic maps and line profiles from data extracted from 2D-FDTD simulations using acoustic properties extracted from a clinical CT dataset. A) PAMs formed with simulated emissions propagating through water only and through the human skull and soft tissue. The effects of including absorption in the simulations and a variable speed of sound (SOS) in the PAM reconstruction were treated separately. In all simulations the synthetic point source had a Gaussian profile, a central frequency of 0.88 MHz, and equal amplitudes. In each PAM, the near field is on the right side of the image (i.e. the US imaging array was on the right). (B) Normalized transverse and axial line profiles for the different conditions tested; i) water-only propagation (Water); ii) propagation through the skull, absorption not included, constant SOS (With Skull W/O Abs. C.SOS); iii) propagation through the skull, absorption included, constant SOS (With Skull W Abs. C.SOS); and iiv) propagation through the skull, absorption included, variable SOS (With Skull W Abs. V.SOS). When a constant sound speed was used, the average value over a line between the synthetic point source and the center of the US imaging array was calculated using Eq. 11. The FWHM values for the different conditions are indicated. The location (0,0) is the coordinate of the point source.

IV. DISCUSSION

The propagation of diverging pressure waves, such as those emitted from oscillating microbubbles, through different media introduces significant distortion and loss which hinders their accurate localization and quantification. Here, we developed a noninvasive framework that is amenable to clinical translation that combines FDTD numerical simulations, realistic modeling of microbubble emissions, and multimodality imaging (US/MR/CT) to transcranially map acoustic cavitation. Our approach also allowed us to refine a standard PAM back-projection algorithm to account for spatially varying wave propagation effects, such as refraction and diffraction and demonstrate its utility with clinical datasets.

In particular, we demonstrated that the PAM back-projection algorithm with a variable speed of sound can substantially reduce the aberration induced by the skull and more accurately localize the source. In addition to correcting for apparent shifts in location of the cavitation activity, this back-projection method appeared to substantially reduce the variability in the PAM intensity for different locations. This ability might explain some of the variations in our past experiments where we found a correlation between the strength of harmonic acoustic emission with MRI contrast agent extravasation after FUS-induced BBB disruption [21]. Being able to accurately take into account the effects of the skull on the recorded emissions could improve this correlation and allow its use regardless of the location of the focus in the brain. In our effort to quantify the emissions and improve these data, we expect that the impact of the bandwidth probe's to the recorded emissions will be particularly important and should be taken into consideration, while a more thorough characterization of the mirror's properties and its impact on the emissions is needed, especially if the proposed set up is to be used in the clinics.

While the scope of the present study was to demonstrate the feasibility in mapping cavitation activity transcranially, future studies can be performed to assess the full spectrum of this technique and compare its benefits and limitations with other similar methods based on the ray-beam approximation [28]. It would also be desirable to perform volumetric PAM with the refined algorithm, which may yield further improvements in resolution and localization accuracy and significantly reduce the number of outliers observed in our previous studies [31]. Moving to three dimensional imaging will also allow us to take into account out of plane emissions and improve the registration accuracy and the safety margin of numerous cavitation based therapies.

While there is no doubt that volumetric (3D) as opposed to planar (2D) imaging will provide significant additional information, we have clearly demonstrated the potential of the present setup to monitor and potentially guide FUS therapies in the brain [31], [36]. The advantage of this approach, as opposed to the system presented by Jones et al [28], is its compatibility with currently available clinical systems, and may thus be useful in accelerating the translation of cavitation based therapies to the clinic. High resolution can still be attained using 95% percentile of the PAM intensity [31], super resolution techniques [32] or by simply increasing the aperture of the array (e.g. ring array) or by combining two arrays (i.e. arranged perpendicularly). The latter can provide 3 mm or less resolution in both directions. This resolution cell is clinically relevant as it matches the transverse profile of the clinical FUS system used in the present study. We also anticipate the there could be cases where a linear array might be more beneficial from spherical, as the spherical arrangement of elements diminishes both the resolution and the sensitivity away of the geometric focus. Finally, given the low powers required for microbubble enhanced therapies in the brain it is not certain that a hemispherical, high gain system is essential for these applications. So, although there is plenty of space for optimization, this arrangement offers numerous benefits and it, thus, could be used in its current or similar form in the clinics.

For moving to the clinic there is also a need to identify and understand all the characteristics and properties of the PAM.

For example, we need to fully understand the origin of the two small grating lobes in the near field of the experimental data, which were not present in the simulations. Further, bubble clouds and in particular the interaction of bubbles may have significant implications to the PAM accuracy. Although, in the experimental data we were able to successfully localize the microbubble activity, which implies constructive interference from numerous bubbles, at higher excitation frequencies destructive interference may be more pronounced. In addition, data with strong broadband emissions may be more challenging to reconstruct, due to the complex scattering profile and the possibility of bubble cloud formations. Part of our future studies is to provide additional and detailed evaluation of these differences using ex-vivo human cadavers. These data will be complemented with simulations that will incorporate emissions from bubble cloud models. This might also be relevant to the data presented here, as our previous work implies that multiple bubbles in the focal region, maybe more than 100, are needed in order to be able to detect the emissions. At these studies we consistently recorded much stronger signals from the more vascular gray matter than the less vascular white matter and when different microbubble concentrations were tested[21].

Our present data imply that the ventricles, as water-filled cavities, and different brain areas (white matter/gray matter) will not have significant impact as they will be overshadowed by the impact of the skull. However, we suspect that these differences will be more pronounced at higher frequencies. A more thorough study that will investigate the impact of these structures in the emissions beam path is needed. We should, however, note that when the recorded emissions propagate through a small part of the skull, which does not incorporate significant variations in thickness and curvature, its effect on the PAM is small and in many cases the use variable sound speed alters only the location of maxima and not the resolution or "shape" of the PAM. The latter emphasizes the reason why imaging from the temporal window is beneficial and explains the very good co-localization between the cavitation activity and its MR-evident bioeffects we found in our previous publications [31]. More work to optimize the position of the array or elements in 3D space is certainly needed. We believe that such optimization will also be part of the treatment planning for each patient separately in order to take into account the specific variations in head shape, thickness, target location etc. We hope that the work presented here will pave the way for such (personalized) planning.

We also plan to develop objective methods to identify the "best" CT slice, as such methods in combination with the information provided by the PAM could also be useful for identifying the emissions' plane, the migration of a bubble could or focal shifts during the sonication, if any. Further improvements can be attained by optimizing our multimodality registration methodology. For example, we anticipate that using higher resolution images and smaller fiducial markers with larger separation will further improve the agreement between simulations and experimental data. Generalization of our framework to other applications beyond the brain (i.e. abdomen) will certainly require real time image-based registration methods that can provide higher accuracy[56]. These registration methods, including the present one, should be evaluated by establishing ground truth target points, measurement of target-registration-error, as well as point source localization using training data sets.

It is important to emphasize that the proposed methodology simply utilizes existing data and does not require additional examinations. For example, the CT data used here are already needed for correcting skull aberration during the sonications. Of course we added the US array and its read out, but we believe that PAM will be an essential part for many FUS procedures. In addition, the application of FUS in the brain necessitates the use for MRI. So, while the need for all these modalities make it an expensive and rather sophisticated treatment, we expect that the clinical outcomes will justify the costs. Also, we believe that the present system that provides the ability to monitor and control all possible interactions of FUS with tissues (thermal and mechanical effects) will be an important research tool for developing new therapies, identifying optimal operation regimes, and establishing safety margins. Ultimately it might be useful in designing FUS systems with the essential components and exams needed, thus reducing the long term costs of this therapeutic procedure.

While additional work is required, overall the simulations and data collected so far support our hypothesis that the strength of the microbubble emissions, which echo the strength of the oscillations, can be used to modulate cavitation induced bioeffects non-invasively, such as the level of the BBB disruption. We anticipate that further improvements in the monitoring could be revealed by improving upon the numerical simulations of the microbubble acoustic emissions. For example, the method can be further refined to incorporate i) frequency-dependent absorption, ii) numerical excitation of multiple microbubbles or microbubble clouds using the acoustic field of the FUS transducer, iii) nonlinearities in the propagation of the excitation pulse, iv) the exact properties of the US imaging array (frequency response, etc.), and in the case where a microbubble agent is used, v) a three-dimensional model of the microvasculature. In addition, we expect that in some situations, such as when the target is close to the skull, that it will be important to include shear waves and mode conversion in both the simulations of the microbubble emissions and in the PAM reconstruction method. In our view, the development of effective methods to monitor and control the procedure is critical for the widespread clinical translation of this promising drug delivery technique. Other microbubble-enhanced therapies, such as cavitation-enhanced thermal ablation [36] and sonothrombolysis [16], can also benefit from this technique.

Our long-term goal is to be able to accurately estimate the cellular or microvascular perturbations induced by oscillating microbubbles in order to develop translational tools for therapeutic and diagnostic applications that harness acoustic cavitation. We anticipate that if the acoustic propagation is correctly taken into account, it will ultimately be possible to relate the intensity in passive acoustic map to the forces that the oscillating microbubbles exert on adjacent structures (vessels, tissues, etc.). We envision that this ability will provide control over this inherently nonlinear process and will result in more precise, more controlled and more effective therapies in the brain.

V. CONCLUSION

A full three-dimensional FDTD simulation for heterogeneous absorbing mediums was used to assess the losses and aberrations of microbubble acoustic emissions propagating through a NHP skull and towards a virtual US imaging array. The FDTD simulations, which used multimodality imaging co-registration (US/MR/CT) to provide accurate determination of the acoustic properties and confluence with the experimental conditions, enabled us to i) implement and test the localization accuracy of synthetic point sources of a standard PAM back-projection algorithm that was refined to incorporate a variable speed of sound (29% and 39% disparity in FWHMs compared to water-only propagation), ii) assess the losses of the microbubble's emissions as they propagated toward the receivers (70% out of 95% of total loss in intensity is due to reflections and scatter), and iii) compare a simulated and experimental PAM (>94% agreement in the FWHMs). We also showed that reconstructing the maps with a variable speed of sound reduced the intensity variation from location-to-location, and we performed a simulation that suggests that it can be used under clinical conditions. Overall, we anticipate that such methods can lead to a more quantitative analysis of microbubble activity in the brain and will improve our ability to monitor and control cavitation-based therapies.

VI. ACKNOWLEDGEMENTS

The authors would like to thank Dr Andriy Fedorov for his help with the software 3D Slicer and image registration. InSightec provided the TcMRgFUSsystem.

REFERENCES

[1] J. Park, Z. Fan, R. E. Kumon, M. E. H. El-Sayed, and C. X. Deng, “Modulation of intracellular Ca2+ concentration in brain microvascular endothelial cells in vitro by acoustic cavitation,” *Ultrasound Med. Biol.*, vol. 36, no. 7, pp. 1176–1187, Jul. 2010.

[2] K. Tachibana, T. Uchida, K. Ogawa, N. Yamashita, and K. Tamura, “Induction of cell-membrane porosity by ultrasound,” *Lancet*, vol. 353, p. 1409, Apr. 1999.

[3] P. Prentice, A. Cuschieri, K. Dholakia, M. Prausnitz, and P. Campbell, “Membrane disruption by optically controlled microbubble cavitation,” *Nature*, vol. 1, pp. 107–111, 2005.

[4] K. Hynynen, N. McDannold, N. Vykhodtseva, and F. A. Jolesz, “Noninvasive MR imaging-guided focal opening of the blood-brain barrier in rabbits,” *Radiology*, vol. 220, pp. 640–6, Sep. 2001.

[5] S. J. Monteith, N. F. Kassell, O. Goren, and S. Harnof, “Transcranial MR-guided focused ultrasound sonothrombolysis in the treatment of intracerebral hemorrhage,” *Neurosurg. Focus*, vol. 34, no. 5, p. E14, May 2013.

[6] S. D. Sokka, R. King, and K. Hynynen, “MRI-guided gas bubble enhanced ultrasound heating in in vivo rabbit thigh,” *Phys Med Biol*, vol. 48, pp. 223–41, Jan. 2003.

[7] R. G. Holt and R. A. Roy, “Measurements of bubble-enhanced heating from focused, MHz-frequency ultrasound in a tissue-mimicking material,” *Ultrasound Med Biol*, vol. 27, pp. 1399–412, Oct. 2001.

[8] Z. Xu, A. Ludomirsky, L. Y. Eun, T. L. Hall, B. C. Tran, J. B. Fowlkes, and C. A. Cain, “Controlled Ultrasound Tissue Erosion,” *IEEE Trans. Ultrason. Ferroelectr. Freq. Control*, vol. 51, no. 6, p. 726, Jun. 2004.

[9] M. Kinoshita, N. McDannold, F. A. Jolesz, and K. Hynynen, “Noninvasive localized delivery of Herceptin to the mouse brain by MRI-guided focused ultrasound-induced blood-brain barrier disruption,” *Proc Natl Acad Sci U A*, vol. 103, pp. 11719–23, Aug. 2006.

[10] J. J. Choi, K. Selert, F. Vlachos, A. Wong, and E. E. Konofagou, “Noninvasive and localized neuronal delivery using short ultrasonic pulses and microbubbles,” *Proc. Natl. Acad. Sci.*, vol. 108, no. 40, pp. 16539–16544, Oct. 2011.

[11] S. Hilgenfeldt, D. Lohse, and M. Zomack, “Sound scattering and localized heat deposition of pulse-driven microbubbles,” *J Acoust Soc Am*, vol. 107, pp. 3530–9, Jun. 2000.

[12] V. I. Ilyichev, V. L. Koretz, and N. P. Melnikov, “Spectral characteristics of acoustic cavitation,” Nov-1989.

[13] T. G. Leighton, *The acoustic bubble*. San Diego: Academic Press, 1997.

[14] S. I. Madanshetty, R. A. Roy, and R. E. Apfel, “Acoustic microcavitation: its active and passive acoustic detection,” *J Acoust Soc Am*, vol. 90, pp. 1515–26, Sep. 1991.

[15] A. A. Atchley, L. A. Frizzell, R. E. Apfel, C. K. Holland, S. Madanshetty, and R. A. Roy, “Thresholds for cavitation produced in water by pulsed ultrasound,” *Ultrasonics*, vol. 26, pp. 280–5, Sep. 1988.

[16] S. Datta, C. C. Coussios, L. E. McAdory, J. Tan, T. Porter, G. De Courten-Myers, and C. K. Holland, “Correlation of cavitation with ultrasound enhancement of thrombolysis,” *Ultrasound Med Biol*, vol. 32, pp. 1257–67, Aug. 2006.

[17] C. H. Farny, R. Glynn Holt, and R. A. Roy, “The correlation between bubble-enhanced HIFU heating and cavitation power,” *IEEE Trans Biomed Eng*, vol. 57, pp. 175–84, Jan. 2009.

[18] C. D. Arvanitis, M. Bazan-Peregrino, B. Rifai, L. W. Seymour, and C. C. Coussios, “Cavitation-Enhanced Extravasation for Drug Delivery,” *Ultrasound Med. Biol.*, vol. 37, no. 11, pp. 1838–1852, Nov. 2011.

[19] N. McDannold, N. Vykhodtseva, and K. Hynynen, “Targeted disruption of the blood-brain barrier with focused ultrasound: association with cavitation activity,” *Phys Med Biol*, vol. 51, pp. 793–807, Feb. 2006.

[20] Y. S. Tung, F. Vlachos, J. J. Choi, T. Deffieux, K. Selert, and E. E. Konofagou, “In vivo transcranial cavitation threshold detection during ultrasound-induced blood-brain barrier opening in mice,” *Phys Med Biol*, vol. 55, pp. 6141–55, Oct. 2010.

[21] C. D. Arvanitis, M. S. Livingstone, N. Vykhodtseva, and N. McDannold, “Controlled Ultrasound-Induced Blood-Brain Barrier Disruption Using Passive Acoustic Emissions Monitoring,” *PLoS ONE*, vol. 7, no. 9, p. e45783, Sep. 2012.

[22] M. Bazan-Peregrino, C. D. Arvanitis, B. Rifai, L. W. Seymour, and C.-C. Coussios, “Ultrasound-induced cavitation enhances the delivery and therapeutic efficacy of an oncolytic virus in an in vitro model,” *J. Controlled Release*, vol. 157, no. 2, pp. 235–242, Jan. 2012.

[23] N. Rapoport, Z. Gao, and A. Kennedy, “Multifunctional nanoparticles for combining ultrasonic tumor imaging and targeted chemotherapy,” *J Natl Cancer Inst*, vol. 99, pp. 1095–106, Jul. 2007.

[24] S. J. Norton, B. J. Carr, and A. J. Witten, “Passive imaging of underground acoustic sources,” *J Acoust Soc Am*, vol. 119, pp. 2840–2847, 2006.

[25] V. A. Salgaonkar, S. Datta, C. K. Holland, and T. D. Mast, “Passive cavitation imaging with ultrasound arrays,” *J. Acoust. Soc. Am.*, vol. 126, no. 6, pp. 3071–3083, 2009.

[26] M. Gyongy and C. C. Coussios, “Passive spatial mapping of inertial cavitation during HIFU exposure,” *IEEE Trans Biomed Eng*, vol. 57, pp. 48–56, Jan. 2010.

[27] K. J. Haworth, T. D. Mast, K. Radhakrishnan, M. T. Burgess, J. A. Kopechek, S. L. Huang, D. D. McPherson, and C. K. Holland, “Passive imaging with pulsed ultrasound insonations,” *J Acoust Soc Am*, vol. 132, pp. 544–53, Jul. 2012.

[28] R. M. Jones, M. A. O’Reilly, and K. Hynynen, “Transcranial passive acoustic mapping with hemispherical sparse arrays using CT-based skull-specific aberration corrections: a simulation study,” *Phys. Med. Biol.*, vol. 58, no. 14, p. 4981, Jul. 2013.

[29] J. Gateau, J. F. Aubry, M. Pernot, M. Fink, and M. Tanter, “Combined passive detection and ultrafast active imaging of cavitation events

induced by short pulses of high-intensity ultrasound," *IEEE Trans Ultrason Ferroelectr Freq Control*, vol. 58, pp. 517–32, Mar. 2011.

[30] C. R. Jensen, R. W. Ritchie, M. Gyongy, J. R. Collin, T. Leslie, and C. C. Coussios, "Spatiotemporal monitoring of high-intensity focused ultrasound therapy with passive acoustic mapping," *Radiology*, vol. 262, pp. 252–61, Jan. 2012.

[31] C. D. Arvanitis, M. S. Livingstone, and N. McDannold, "Combined ultrasound and MR imaging to guide focused ultrasound therapies in the brain," *Phys. Med. Biol.*, vol. 58, no. 14, p. 4749, Jul. 2013.

[32] M. A. O'Reilly and K. Hynynen, "A super-resolution ultrasound method for brain vascular mapping," *Med. Phys.*, vol. 40, no. 11, p. 110701, Oct. 2013.

[33] M. OReilly, R. Jones, and K. Hynynen, "Three-Dimensional Transcranial Ultrasound Imaging of Microbubble Clouds Using a Sparse Hemispherical Array," *IEEE Trans. Biomed. Eng.*, vol. Early Access Online, 2014.

[34] G. T. Clement and K. Hynynen, "A non-invasive method for focusing ultrasound through the human skull," *Phys. Med. Biol.*, vol. 47, no. 8, p. 1219, Apr. 2002.

[35] J.-F. Aubry, M. Tanter, M. Pernot, J.-L. Thomas, and M. Fink, "Experimental demonstration of noninvasive transskull adaptive focusing based on prior computed tomography scans," *J. Acoust. Soc. Am.*, vol. 113, no. 1, pp. 84–93, 2003.

[36] C. D. Arvanitis and N. McDannold, "Integrated ultrasound and magnetic resonance imaging for simultaneous temperature and cavitation monitoring during focused ultrasound therapies," *Med. Phys.*, vol. 40, no. 11, p. 112901, Oct. 2013.

[37] Y. Jing, F. C. Meral, and G. T. Clement, "Time-reversal transcranial ultrasound beam focusing using a k-space method," *Phys. Med. Biol.*, vol. 57, no. 4, p. 901, Feb. 2012.

[38] B. E. Treeby, J. Jaros, A. P. Rendell, and B. T. Cox, "Modeling nonlinear ultrasound propagation in heterogeneous media with power law absorption using a k-space pseudospectral method," *J. Acoust. Soc. Am.*, vol. 131, no. 6, pp. 4324–4336, Jun. 2012.

[39] I. M. Hallaj and R. O. Cleveland, "FDTD simulation of finite-amplitude pressure and temperature fields for biomedical ultrasound," *J. Acoust. Soc. Am.*, vol. 105, no. 5, pp. L7–L12, Mar. 1999.

[40] C. W. Connor and K. Hynynen, "Patterns of thermal deposition in the skull during transcranial focused ultrasound surgery," *IEEE Trans. Biomed. Eng.*, vol. 51, no. 10, pp. 1693–1706, 2004.

[41] C. C. Church, "The effects of an elastic solid surface layer on the radial pulsations of gas bubbles," *J. Acoust. Soc. Am.*, vol. 97, no. 3, pp. 1510–1521, Mar. 1995.

[42] L. Hoff, P. C. Sontum, and J. M. Hovem, "Oscillations of polymeric microbubbles: Effect of the encapsulating shell," *J. Acoust. Soc. Am.*, vol. 107, no. 4, pp. 2272–2280, Apr. 2000.

[43] S. J. Norton and I. J. Won, "Time exposure acoustics," *IEEE Trans Geosci Rem Sens*, vol. 38, pp. 1337–1343, 2000.

[44] N. McDannold, G. T. Clement, P. Black, F. Jolesz, and K. Hynynen, "Transcranial magnetic resonance imaging- guided focused ultrasound surgery of brain tumors: initial findings in 3 patients," *Neurosurgery*, vol. 66, pp. 323–32, Feb. 2010.

[45] D. T. Blackstock, *Fundamentals of physical acoustics*. New York: Wiley, 2000.

[46] M. F. Hamilton and D. T. Blackstock, *Nonlinear Acoustics*. Academic Press, 1998.

[47] K. Yee, "Numerical solution of initial boundary value problems involving maxwell's equations in isotropic media," *IEEE Trans. Antennas Propag.*, vol. 14, no. 3, pp. 302–307, 1966.

[48] C. de Groot–Hedlin, "Finite-difference time-domain synthesis of infrasound propagation through an absorbing atmosphere," *J. Acoust. Soc. Am.*, vol. 124, no. 3, pp. 1430–1441, Sep. 2008.

[49] A. Taflove and S. C. Hagness, *Computational electrodynamics: the finite-difference time-domain method*. Boston: Artech House, 2005.

[50] G. F. Pinton, J. Dahl, S. Rosenzweig, and G. E. Trahey, "A heterogeneous nonlinear attenuating full- wave model of ultrasound," *IEEE Trans. Ultrason. Ferroelectr. Freq. Control*, vol. 56, no. 3, pp. 474–488, 2009.

[51] R. Mettin, I. Akhatov, U. Parlitz, C. D. Ohl, and W. Lauterborn, "Bjerknes forces between small cavitation bubbles in a strong acoustic field," *Phys. Rev. E*, vol. 56, no. 3, pp. 2924–2931, Sep. 1997.

[52] L. A. Crum, "Bjerknes forces on bubbles in a stationary sound field," *J. Acoust. Soc. Am.*, vol. 57, no. 6, pp. 1363–1370, Jun. 1975.

[53] C. D. Arvanitis and N. McDannold, "Simultaneous temperature and cavitation activity mapping with a transcranial MR-guided focused ultrasound system," *Proc IEEE Int. Ultrason. Sumpos.*, pp. 128 – 131, 2011.

[54] F. Marquet, M. Pernot, J.-F. Aubry, G. Montaldo, L. Marsac, M. Tanter, and M. Fink, "Non-invasive transcranial ultrasound therapy based on a 3D CT scan: protocol validation and in vitro results," *Phys. Med. Biol.*, vol. 54, no. 9, p. 2597, May 2009.

[55] N. McDannold, C. D. Arvanitis, N. Vykhodtseva, and M. S. Livingstone, "Temporary disruption of the blood-brain barrier by use of ultrasound and microbubbles: safety and efficacy evaluation in rhesus macaques," *Cancer Res*, vol. 72, pp. 3652–63, Jul. 2012.

[56] W. Wein, S. Brunke, A. Khamene, M. R. Callstrom, and N. Navab, "Automatic CT-ultrasound registration for diagnostic imaging and image-guided intervention," *Med. Image Anal.*, vol. 12, no. 5, pp. 577–585, Oct. 2008.